Proceedings of Global Power and Propulsion Society
ISSN-Nr: 2504-4400
GPPS Hong Kong 2023
October 17-19, 2023
www.gpps.global

GPPS-TC-2023-Put 4 digit paper number here (i.e. GPPS-TC-2023-0189)

Jet Installation Noise Modelling for Subsonic Round and Chevron Jets

Hussain A. Abid
Queen Mary, University of London
h.abid@qmul.ac.uk
London, United Kingdom

Annabel P. Markesteijn
Queen Mary, University of London
a.p.markesteijn@gmail.com
London, United Kingdom

Sergey A. Karabasov
Queen Mary, University of London
s.karabasov@qmul.ac.uk
London, United Kingdom

Hasan K. Jawahar
University of Bristol
hasan.kj@bristol.ac.uk
Bristol, United Kingdom

Mahdi Azarpeyvand
University of Bristol
m.azarpeyvand@bristol.ac.uk
Bristol, United Kingdom

ABSTRACT

Jet mixing and installation noise remains one of the leading sources of community noise during the take-off phase. Previously, chevron nozzles were primarily used as a noise reduction technology for isolated jet noise. However, a systematic investigation of chevron nozzles in installed configurations is lacking. The present work partly fulfils this gap by investigating the effect of chevron nozzle geometry on jet mixing and installation noise for a round and two chevron nozzles at subsonic Mach numbers from 0.3 to 0.9. The installed jet configuration follows a series of experiments conducted at the University of Bristol, with the plate located in the linear hydrodynamic field of the jet. Unsteady flow solutions are obtained using the high-resolution CABARET method in the Wall Model Large Eddy Simulation regime and accelerated on Graphics Processing Units. Far-field noise for the installed jet is calculated using both the permeable and impermeable surface formulation of the Ffowcs Williams - Hawkings method to analyse the importance of quadrupole and dipole sources depending on the nozzle geometry, acoustic Mach number, and observer angle. The numerical predictions of the installed and isolated jets are compared with each other, as well as with experimental data. In each case, insights into noise generation mechanisms are discussed.

INTRODUCTION

The reduction of noise generated by high-speed propulsive jet engines has been a significant challenge in the field of aeroacoustics since the advent of jet engine aircraft. A significant contributor to the overall noise produced by an aircraft is jet noise, which is proportional to a high power of the jet flow velocity (Jordan et al., 2018). The introduction of high-bypass ratio (HBR) engines led to a decrease in jet noise levels, particularly during take-off, as HBR technology results in a reduction in exhaust jet velocity without reducing aerodynamic performance (Hoheisel and Frhr. von Geyr, 2012). However, the implementation of HBR technology aircraft engines resulted in an increase in engine nacelle diameter and positioning of the engine in close proximity to the wing in order to maintain adequate ground clearance. Consequently, this led to the interaction of the jet near-field with the air-frame, resulting in an additional noise source known as jet-installation (JI) noise. Several studies (Head R., n.d.; Mead and Strange, 1998; Lawrence et al., 2011) have demonstrated that JI noise is characterised by low and mid-frequency amplification, which dominates during take-off, especially when the jets at high power interacts with deployed high-lift devices.

One of the mechanisms of JI noise is attributed to the scattering of the hydrodynamic pressure field in the vicinity of the jet caused by the solid surface. Unlike the acoustic field generated by jet mixing, which results from turbulence-turbulence interactions, the hydrodynamic pressure field in isolated jets is evanescent, and decays exponentially in the radial direction. However, the presence of the scattering surface leads to its efficient propagation to the far field (Lyu and Dowling, n.d.). Studies conducted by (Head R., n.d.; Way and Turner, 1980; Shearin, 1983; Mead and Strange, 1998; Lyu and Dowling, n.d.) indicate the near-field jet hydrodynamic pressure scattering by the edge of the solid surface displays dipole properties. This suggests that reducing JI noise may require modifying the near-jet characteristics of the hydrodynamic pressure, such

as reducing the spectral amplitude that corresponds to the pressure correlation length scale and convection velocity. (Lyu and Dowling, n.d.).

A popular jet noise reduction technology is using chevron nozzles to increase jet mixing, thereby breaking the coherent jet structures which contribute to peak jet noise radiation (Brown and Wernet, 2014; Jawahar et al., n.d.; Kamliya Jawahar et al., 2023). The noise reduction performance of chevron nozzles depends on several parameters, which include the number of chevrons and penetration angle. For example, in an experimental investigation by NASA (Bridges and Brown, n.d.) into the noise modification characteristics of chevron nozzles for isolated jets, it was observed that the chevron enhances large-scale mixing, thereby modifying the large-scale coherent structures of the jet that contribute to low-frequency noise. More recently, (Jawahar et al., n.d.) performed extensive experimental investigation using several round and chevron nozzles of similar profiles to the NASA SMC series. A particular focus of that investigation was on the low-frequency content of the noise spectrum for isolated and installed jets.

In this work, several jets previously considered in the experiment of (Jawahar et al., n.d.) is simulated numerically using a Wall Modelled LES (WMLES) method coupled with the Ffowcs Williams-Hawkings technique for far-field noise propagation. The WMLES calculations performed in this work are based on the high-resolution CABARET method (Karabasov and Goloviznin, 2009; Tucker and Karabasov, 2009; Chintagunta et al., 2018; Semiletov and Karabasov, 2013) accelerated on Graphics Processing Units (GPU) (Markesteijn and Karabasov, 2018). The solver utilizes a GPU-optimized method for solving the hyperbolic part of the Navier-Stokes equations, using asynchronous time stepping at the optimal CFL number corresponding to a minimum dispersion and dissipation error (Semiletov and Karabasov, 2013, 2014). The CABARET method for jet flow and noise calculations was validated in previous studies (Faranosov et al., 2013; Semiletov and Karabasov, 2018; Markesteijn and Karabasov, 2019; Markesteijn et al., 2020) and for airfoil flows in (Abid, Markesteijn and Karabasov, 2021; Abid, Stalnov and Karabasov, 2021).

The aims of the simulations are to first validate the GPU-CABARET solutions for a range of installed chevron nozzle geometries in comparison with the baseline round jet against the experiment. Then these solutions will be used to characterise the noise generation mechanisms in each case, subject to the jet acoustic Mach number, observer angle, nozzle geometry, and jet installation effect.

1 NUMERICAL SETUP

1.1 Installed jet configuration and flow condition

The installed jet configuration and flow conditions examined in this study are based on experiments conducted at the University of Bristol's Jet Aeroacoustics Research Facility (B-JARF), where isolated jets are positioned in close proximity to a flat plate (Jawahar et al., n.d.). The test facility has been validated for a wide range of Mach numbers (Kamliya Jawahar, Baskaran and Azarpeyvand, 2021; Kamliya Jawahar, Meloni, Camussi and Azarpeyvand, 2021; Kamliya Jawahar and Azarpeyvand, 2021, 2022) and for many acoustic setups. The background noise is measured in the acoustic chamber and the overall noise measurement by the jet are calibrated in accordance with the background noise. More details of the (B-JARF) can be found in Kamliya Jawahar and Azarpeyvand (2022).

The experimental setup employed a round convergent nozzle (SMC000) and four chevron nozzles; however, this study considers only the SMC002 and SMC006 chevron nozzles to investigate the influence of chevrons on the jet's near-field properties and the installed jet case. These two specific nozzles were chosen for investigation as the experiment by (Bridges and Brown, n.d.; Brown, 2013; Brown and Bridges, 2006) showed that SMC002 results in an increased noise while SMC006 results in decreased noise for the jet in isolated configuration. The purpose of this investigation is to determine whether SMC002 still leads to increased noise and if SMC006 continues to result in decreased noise when the jet is set up in its installed configuration. Fig. 1 shows the round (SMC000) and chevron (SMC002 and SMC006) nozzle. The SMC002 has 4 sawtooth which penetrate into the flow at 5-degree while SMC006 have 6 sawtooth which penetrate into the flow at 18 degree. More details of various chevron is provided in (Brown, 2013).

The nozzles used in the experiments of (Jawahar et al., n.d.) are 3:1 scaled-down versions of the nozzle employed in NASA investigations (Bridges and Brown, n.d.; Brown, 2013; Brown and Bridges, 2006), with an exit jet diameter of $D_j = 16.93mm$ utilized for the present analysis. The experiments conducted by (Bridges and Brown, n.d.; Brown, 2013; Brown and Bridges, 2006) were limited to Mach numbers of 0.5 and 0.9. Their primary objective was to explore the high-frequency components of noise spectra in an isolated configuration. However, the use of the smaller scaled nozzle was employed to investigate the low-frequency part of the noise spectrum, which holds significance for jet in installed setup.

To investigate the installed jet configuration, a flat-plate is installed underneath the jet. In order to avoid the leading-edge and side-edge sound scattering, the flat plate has a length of $4.5D_j$ upstream of the nozzle exit and a semi-span length of $12D_j$. The experimental and numerical simulation setups for the installed jet involve placing the trailing edge of the plate at $L = 6.5D_j$ downstream of the nozzle exit. The distance between the jet centerline and the plate is set to $H = 2D_j$, to ensure that the plate is located in the linear-hydrodynamic field, and any installation effect is caused by the hydrodynamic pressure scattering at the trailing edge.

The present study investigates seven nozzle exit Mach numbers, ranging from 0.3 to 0.9, and extends on the work by (Bridges and Brown, n.d.; Brown, 2013; Brown and Bridges, 2006), where the study was limited to 0.5 and 0.9 nozzle exit

Mach numbers. These Mach numbers are obtained by setting the total pressure and temperature at $4D_j$ upstream of the nozzle exit plane, using nozzle flow equations. In addition, the inlet conditions for Mach 0.5 and 0.9, corresponding to set points 03 and 07 respectively, are determined using values from NASA wind tunnel experiments conducted by Bridges and Brown (Brown and Bridges, 2006). The jet flow conditions and inputs are presented in Table 1, where P_o denotes stagnation pressure, and T_o denotes stagnation temperature. The ambient pressure is set equal to atmospheric pressure, with a value of 101325 Pa, and the ambient temperature is 288.15 K, as reported by Bridges and Brown (Brown and Bridges, 2006). The nozzle's shape and the setup of the installed jet case are depicted in Fig. 1 and Fig. 2, respectively.

Table 1 Conditions of the jet cases from the experiment of (Jawahar et al., n.d.)

Mach Number	Stagnation Pressure P_o (kPa)	Stagnation Temperature T_o (K)
0.3	107.54	263.93
0.4	112.81	267.56
0.5	121.29	273.74
0.6	128.87	277.93
0.7	140.14	284.67
0.8	154.01	292.44
0.9	188.57	292.31

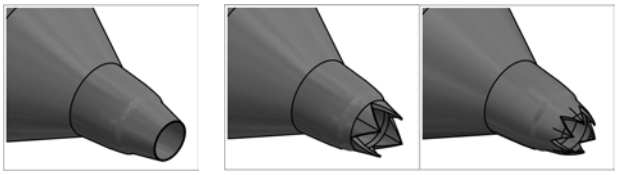

(a) (b) (c)

Figure 1 Nozzle Shapes (a) SMC000 (b) SMC002 (c) SMC006

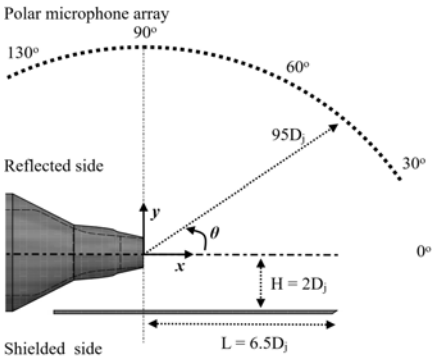

Figure 2 Schematic of the jet-installation setup with $L = 6.5D_j$ and $H = 2D_j$

1.2 GPU Cabaret LES Solver

The numerical simulation of isolated and installed jet cases is performed with an in-house Compact Accurately Boundary-Adjusting High-Resolution Technique (CABARET) LES solver (Faranosov et al., 2013; Semiletov and Karabasov, 2018; Markesteijn and Karabasov, 2019; Markesteijn et al., 2020). The LES solver is based on a low-dispersion, low-dissipation CABARET scheme for solving compressible flows and is coupled with an equilibrium wall model based on the work of Parks (Park, 2015).

The procedure for implementing the WMLES algorithm in the solver involves the following steps. The cell-centred values of velocity (and density) are calculated at each time step within the boundary layer mesh. These values are then supplied to the wall model, which calculates the wall shear stress. This wall shear stress serves as the boundary condition for the LES calculation at the wall. The wall model used in this study is based on the algebraic method and uses Reichardt's law, as described in (Mukha et al., 2019). This law of the wall provides a relationship between the local u^+ and y^+ at the wall and assumes that the instantaneous velocity can be used as input for the wall law. The resulting nonlinear algebraic equation for the velocity profile is solved through a simple Newton iteration, yielding the wall shear stress.

In addition, an explicit asynchronous time-stepping method, as detailed in (Semiletov and Karabasov, 2013, 2014), is utilized to progress the flow solution in an optimal manner with a Courant-Friedrichs-Lewy (CFL) number. The method employs a hierarchy of local time steps that are based on the local cell size, making it highly efficient for simulations involving non-uniform meshes, which are frequently used in simulations of viscous flow. Furthermore, the implementation of the solver, CABARET, has a low memory footprint and is optimized for use on GPUs, leading to an increase in computational speed and reduced turnaround time. During the simulations, eight-time update groups of the asynchronous time-stepping method were employed, leading to a $2^7 = 128$ increase in time step between the smallest and largest grid cells.

1.3 Mesh Generation

The LES mesh for the isolated and installed jet cases was generated using the snappyHexMesh utility in *OpenFOAM*. The layer thickness near the wall boundary was controlled by adding body-fitted hexahedral layers, and automated meshing was employed. During this process, the distance between the centre of the control volume nearest to the boundary and the boundary was kept within a specified range. The mesh topology was designed to refine the nozzle lip with high-density grid cells, and extra refinement was applied from the nozzle exit to a distance of $30D_j$ in the axial direction. A grid sensitivity study was performed by modifying the grid topology from nozzle exit to $30D_j$ and refinement of the cells at the nozzle lip. The mesh and their corresponding grid sizes for isolated and installed jet cases are explained herein

1.3.1 Isolated Jet

The simulations of the round and chevron nozzles in isolated configurations were conducted using 40 million cells. The grid resolution at the nozzle lip line was different for the two nozzle types. Specifically, for SMC000, the grid near the nozzle lip was almost uniformly cartesian with $dx/D = dy/D = dz/D \approx 0.006$, whereas, for SMC002 and SMC006, the grid resolution at the nozzle lip was $dx/D = dy/D = dz/D = 0.01$. In all cases, the refined grid area was placed in the region where the Ffowcs Williams and Hawking (FW-H) acoustic integral surfaces are situated. For the isolated jet, the FW-H surface has a conical shape with multiple closing discs. The grid resolution for SMC000 yielded a maximum resolved Strouhal number near the nozzle exit and near the end of the potential jet core of $St = 9$ and $St = 4$, respectively, with a resolution of 8 points per acoustic wavelength (p.p.w.). On the other hand, for SMC002 and SMC006, the grid resolution resulted in a maximum resolved Strouhal number of $St = 6$ and $St = 3$ near the end of the potential jet core, respectively. A sensitivity analysis is carried out to assess the grid dependence of the numerical simulations for the cells inside the nozzle. The study is conducted with two grid resolutions, i.e., 8 and 12 points per boundary layer, and the results obtained from both resolutions are compared. The analysis reveals that the difference between the results obtained from the two grid resolutions is negligible. Consequently, for the numerical simulations, a grid resolution of 8 points per boundary layer is deemed appropriate, and these points are placed on the inner surface of the nozzle. The mesh topology and grid for the isolated jet nozzles are illustrated in Fig. 3.

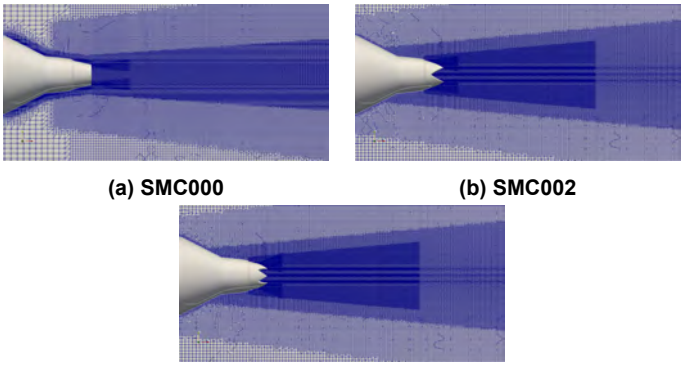

Figure 3 LES grid for the isolated jet configuration (a) SMC000 (b) SMC002 (c) SMC006

1.3.2 Installed jet

The grid resolution for the installed round and chevron jet cases was 40 million grid points. The grid topology for SMC000 near the lip-line and downstream region was similar to that of the isolated SMC000 nozzle, with 8 grid points per boundary layer thickness at the nozzle inlet. The installed chevron nozzles also had a similar grid topology to the isolated nozzle, but the lip line was refined with smaller grid sizes. The grid topology in the downstream location was also varied for installed round and chevron jets and refined in the region of the flow field for FW-H calculation. To ensure adequate resolution of flow structures in the vicinity of the plate, a grid sensitivity analysis was conducted with varying numbers of prism layers near the wall and the maximum thickness of the prism layer. Specifically, two setups were tested with 10

and 4 prism layers near the wall and a maximum thickness of 0.06Dj and an expansion ratio of 1.4. Notably, because the CABARET algorithm uses both the cell-centre and the cell-face variables, the total number of discretization points for 10 and 4 cells in the boundary layer corresponds to 21 and 9, respectively. The GPU-CABARET simulations for these two grid resolutions produced very similar results. Consequently, for the final simulations, a uniform grid with four prism layers was adopted for all installed jet configurations.

1.4 Far-Field Noise Computation

The far-field noise generated by isolated and installed jet simulations using Large Eddy Simulation (LES) is computed by a hybrid computational aeroacoustic (CAA) method. This involves the use of the CABARET LES solver to obtain jet flow parameters, such as fluctuating velocity, density, pressure, and vorticity field, and store them on integral surfaces referred to as Ffowcs Williams-Hawkings (FW-H) surfaces. These parameters are then extrapolated to the far field using the retarded time formulation of the FW-H integral surface method. An illustration of the FW-H surface for the isolated jet modelling is presented in Fig. 4 for SMC006 chevron nozzle, with the FW-H surface positioned outside the jet turbulence and primary vorticity region of the shear layer for noise computation. The noise computation method utilizes 16 integration surfaces, where the LES solution is recorded. Furthermore, the LES grid is refined near the FW-H integral surfaces to enable the computation of dipole, monopole, and quadrupole noise sources. The integral surfaces are treated as permeable, and the momentum and mass flux across the surface contribute to the acoustical field enclosed by the surface.

Two different FW-H methodologies were utilized for the installed jet case to determine the far-field noise. The first method involved coupling the flow solver with a permeable FW-H technique, similar to the modelling of the isolated jet. The FW-H surface, in this case, consisted of the jet region and the plate, as shown in Fig. 5. This comprehensive method includes all quadrupole and dipole jet noise sources. In parallel, an impermeable FW-H formulation was employed, which covered the surface of the plate as the FW-H surface. The impermeable FW-H method only accounts for the noise due to dipole sources. This methodology allowed the separation of the contributions of the dipole and quadrupole noise for JI noise prediction. The noise is computed at polar angles from 20 deg to 120 deg and compared with the experimental measurement by (Jawahar et al., n.d.). The sound pressure level (SPL) and band-limited Overall SPL (OASPL) are compared and discussed in Section 2.

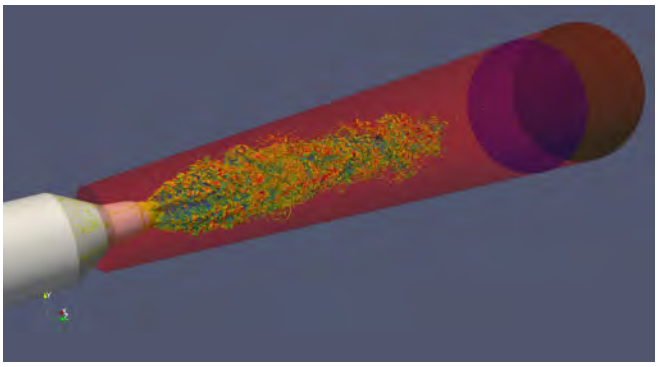

Figure 4 Acoustic integration surfaces wrapped around the vorticity regions of the isolated jet flow for SMC006

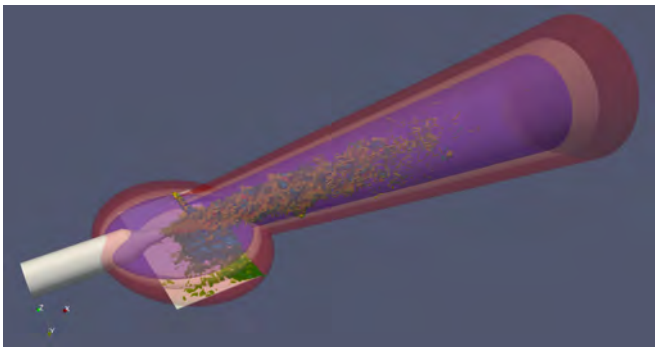

Figure 5 Acoustic integration surfaces wrapped around the vorticity regions of the installed jet flow for SMC006

2 RESULTS AND DISCUSSION

2.1 Jet development and influence of chevrons on the jet flow

This section presents an analysis of the axial and radial evolution of the jet flow field for isolated round and chevron nozzles. Figs. 7 to 10 presents the normalised axial velocity and axial Reynolds stress profiles at various axial distances ($x/D_j = 1, 2, 4, 6, 8$ and 10) in the radial direction ($r/D_j = 3.0$ to -3.0) for Mach numbers 0.5 and 0.9. The LES solution of the isolated SMC000 jet is compared against the experimental PIV measurement from NASA (Bridges and Brown, n.d.), while the profiles for SMC002 and SMC006 are presented for qualitative comparison. The comparison of the round jet with the experimental data shows excellent agreement for both Mach numbers, including the accurate computation of the top-hat velocity profile observed at $x/D_j = 1.0$ to a Gaussian profile until the end of the jet potential core. These results confirm that the LES grid of 40 million cells, along with grid refinement, is sufficient to accurately predict the time-averaged flow profiles.

The study also presents the radial profiles of the normalised axial velocity and axial Reynolds stress for SMC002 and SMC006 chevron nozzles. The results show that the maximum velocity at the jet centerline is similar to that of the round nozzle at axial locations close to the nozzle exit. However, the chevrons induce instability waves that cause the jet to spread radially, as observed in Fig. 6. The velocity contour demonstrates that the chevrons modify the axial velocity flow structure and reduce the potential core length. The potential core length for the round nozzle is approximately 6.0, whereas for the SMC002 chevron nozzle, it is approximately 4.0, and for the SMC006 chevron nozzle, it is approximately 2.5. These results indicate that the chevrons disrupt the large-scale flow structures and shorten the jet's potential core, as evident in instantaneous profile of axial velocity contour shown in Fig. 6. Additionally, the radial spread of the chevron jets is greater than that of the round jet, as evidenced by the well-defined streamlined potential core of the round jet in Fig. 6.

Overall, these findings suggest that the computational mesh configuration consisting of 40 million cells and refined mesh topology around the lip line results in an accurate comparison to the experimental PIV data. The results also demonstrate that the chevrons significantly modify the flow structure, which influences the noise radiated by the jet in isolated and installed setups, as will be discussed in Section 2.2.

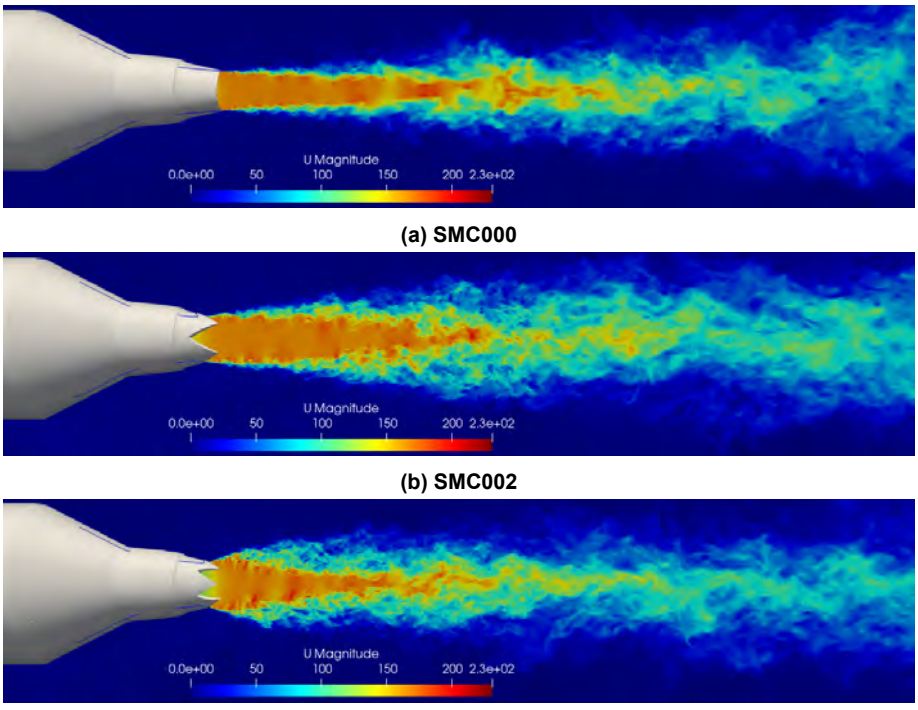

(a) SMC000

(b) SMC002

(c) SMC006

Figure 6 Instantaneous velocity contour for isolated round and chevron nozzles (a) SMC000 (b) SMC002 (c) SMC006

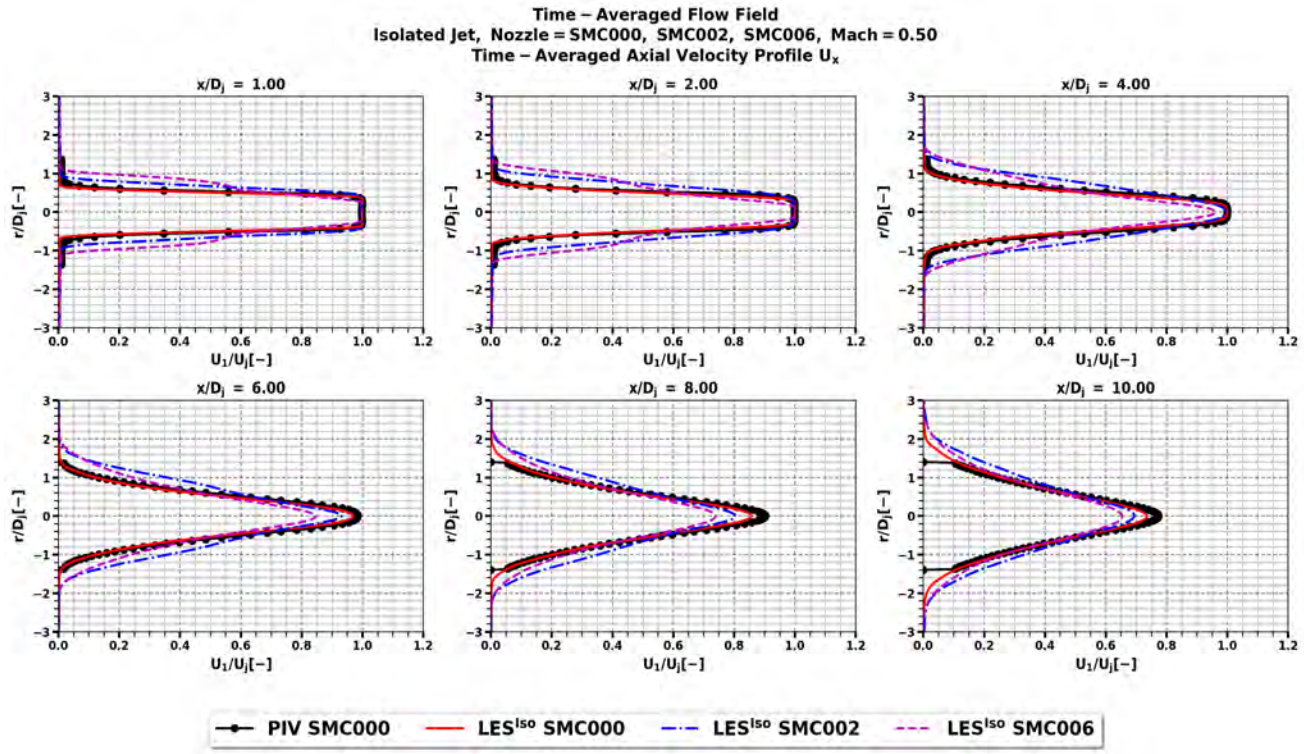

Figure 7 Comparison of the axial Velocity profile at the various axial locations for the isolated SMC000, SMC002 and SMC006 at Mach = 0.5 with the PIV measurement of SMC000.

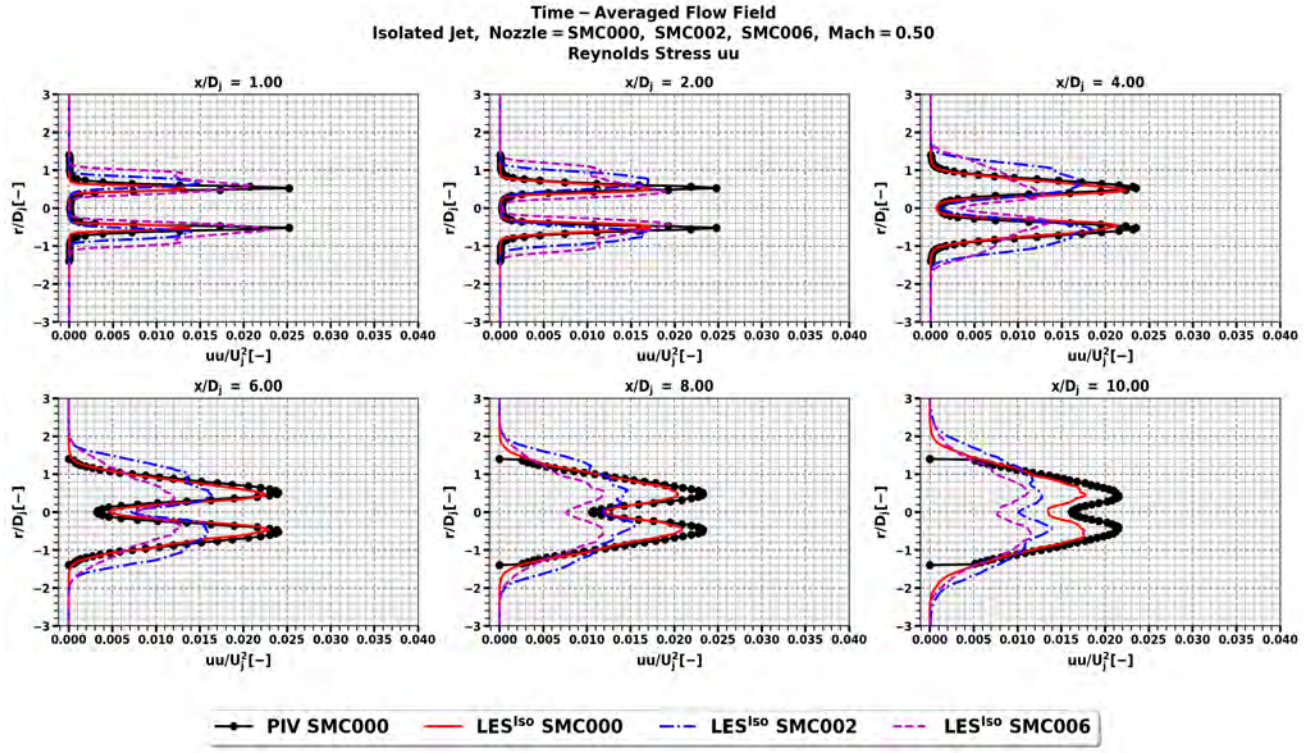

Figure 8 Comparison of the axial Reynolds stress profile at the various axial locations for the isolated SMC000, SMC002 and SMC006 at Mach = 0.5 with the PIV measurement of SMC000.

.

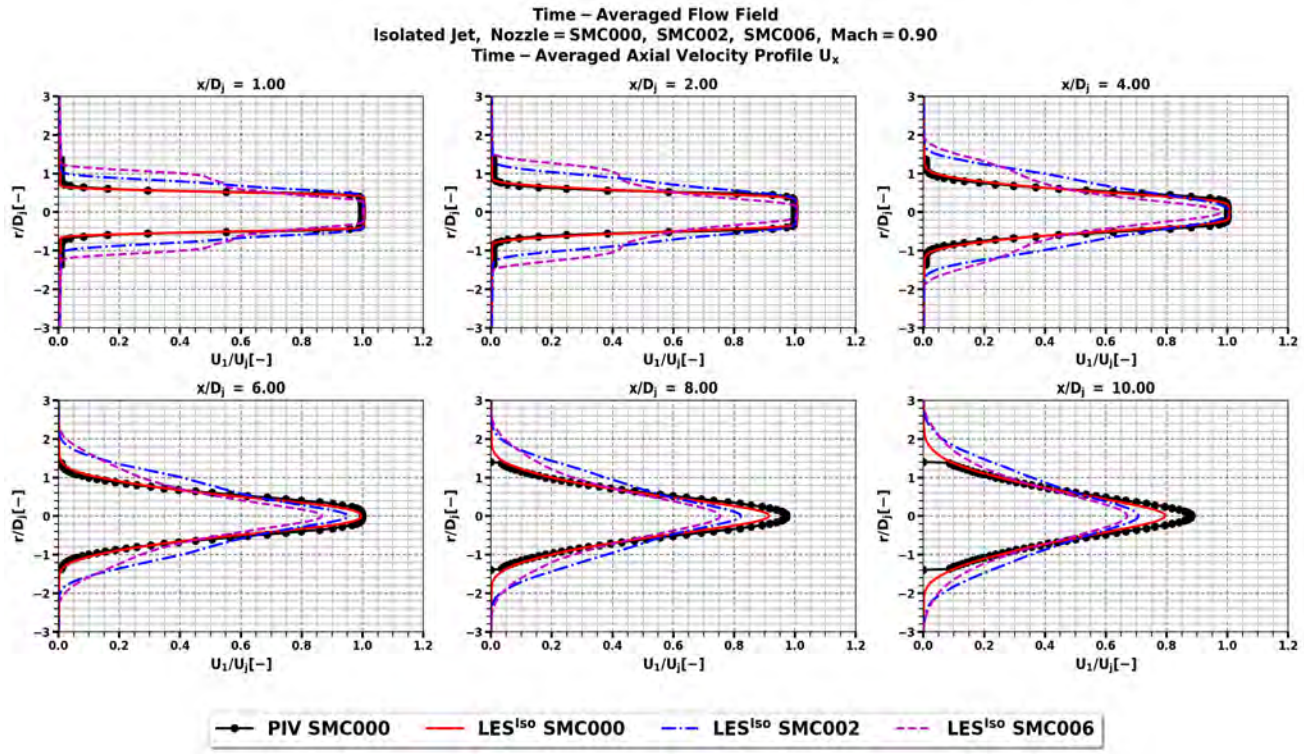

Figure 9 Comparison of the axial Velocity profile at the various axial locations for the isolated SMC000, SMC002 and SMC006 at Mach = 0.9 with the PIV measurement of SMC000.

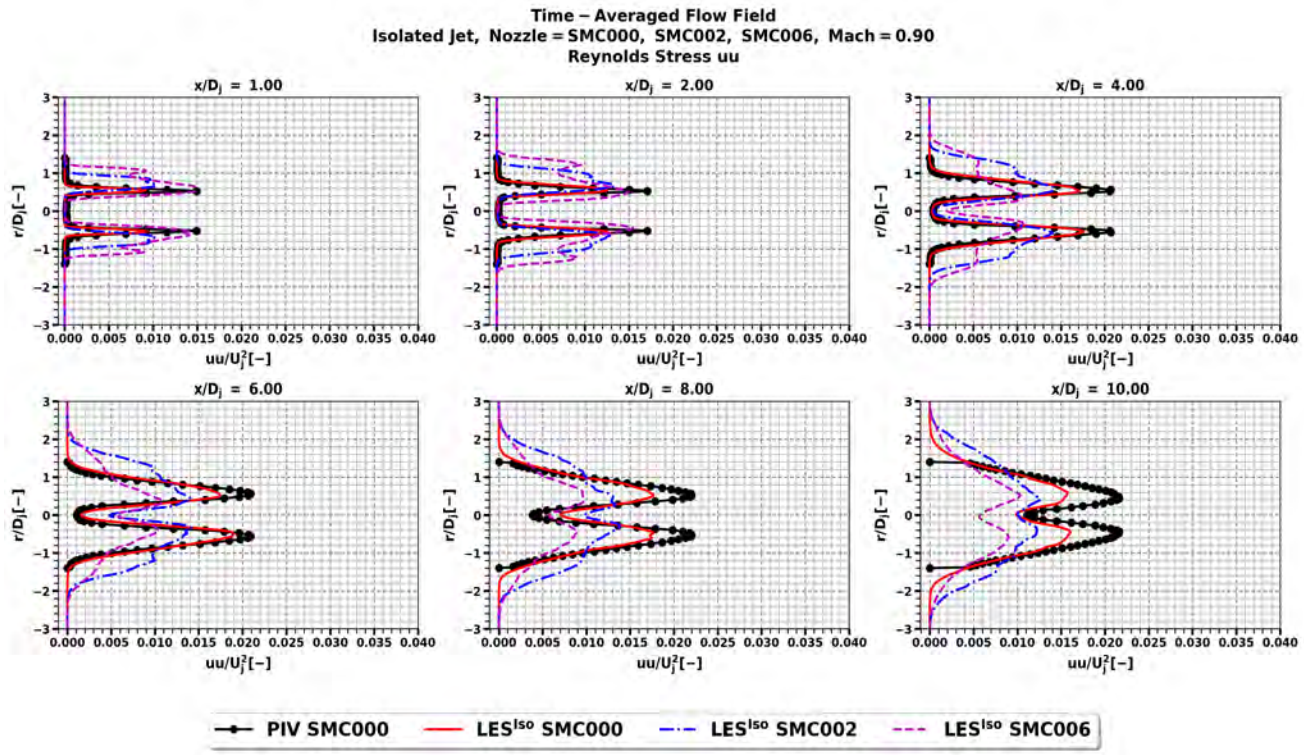

Figure 10 Comparison of the axial Reynolds stress profile at the various axial locations for the isolated SMC000, SMC002 and SMC006 at Mach = 0.9 with the PIV measurement of SMC000.

.

2.2 Far-field Noise Results

This section presents an analysis of the far-field noise computed using LES and FW-H methods for the installed and isolated jet cases of SMC000, SMC002, and SMC006 nozzles over a range of Mach numbers from 0.3 to 0.9. The noise spectra are computed in terms of sound pressure level (SPL) in dB, as defined in Eq. (1). The numerical results for SPL are validated against experimental measurements, followed by the validation of overall sound pressure level (OASPL) in accordance with Eq. (2).

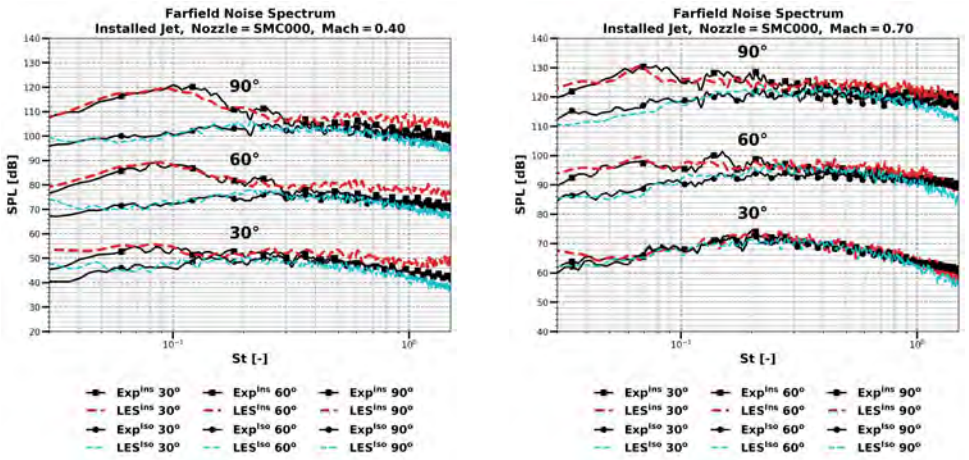

(a) SMC000; M=0.4

(b) SMC000; M=0.7

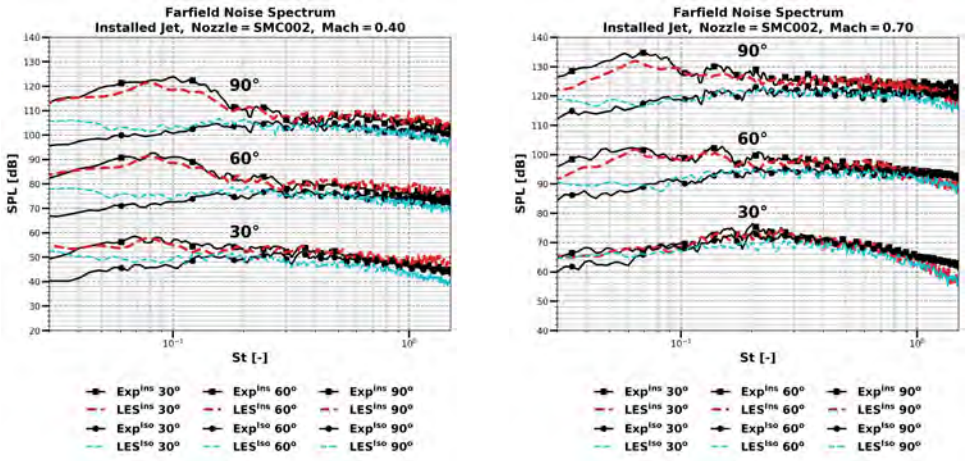

(c) SMC002; M=0.4

(d) SMC002; M=0.7

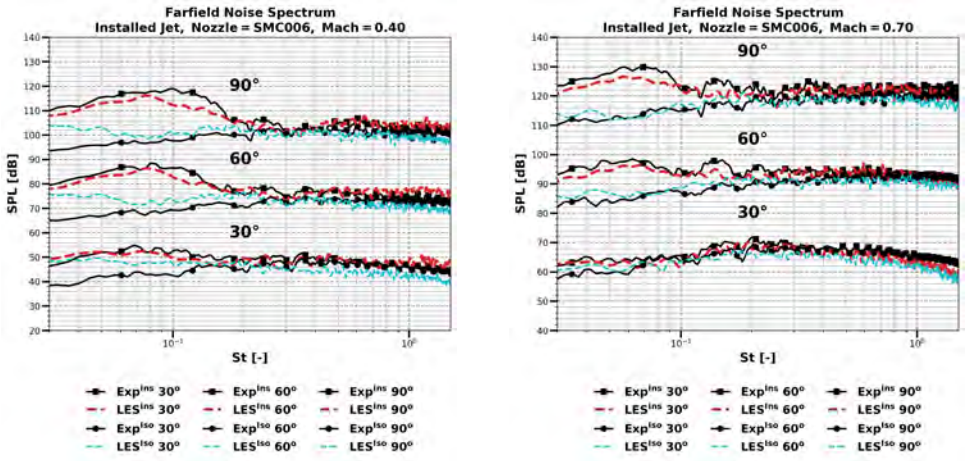

(e) SMC006; M=0.4

(f) SMC006; M=0.7

Figure 11 Comparison of far-field noise using permeable FW-H method for isolated and installed SMC000, SMC002, and SMC006 nozzles at Mach 0.4 and 0.7, with experimental measurements at polar angles of $30°$, $60°$, and $90°$. The spectrum at locations other than $30°$ is shifted by 30dB for clarity.

$$SPL(f) = 10\log_{10}\left(\frac{S_{pp}(f)\times\Delta f}{P_{ref}^2}\right)\left(P_{ref} = 20\times10^{-6}; \Delta f = 2Hz\right) \tag{1}$$

The overall sound pressure level (OASPL) is given by:

$$OASPL = 10\log_{10}\left(\sum_{i=1}^{n}\left(\frac{S_{pp}(f)_i\times\Delta f}{P_{ref}^2}\right)\right), \tag{2}$$

The overall sound pressure level (OASPL) is calculated using the power spectral density (PSD) of the sound pressure signal at each frequency bin. Specifically, $S_{pp}(f)_i$ represents the PSD of the signal at the ith frequency bin, with a frequency resolution of Δf and a total of n frequency bins. The summation is taken over a band-limited range of Strouhal numbers, which are specified using appropriate lower and upper limits. In the current analysis, the Band-Limited OASPL is obtained by averaging the PSDs over a range of 0.04 to 1 Strouhal for both isolated and installed jet setups.

The prediction of the noise radiated by the jet installed underneath the plate is calculated and compared with experimental measurements in Fig. 11. To compute the noise from the LES for the installed jet, two formulations of retarded time FW-H method are utilized: the permeable FW-H method and the impermeable FW-H method. The permeable FW-H method involves multiple integral surfaces that enclose the vorticity field of the jet and plate, and in this study, 16 integral surfaces were selected. The computed noise is the average of the noise calculated from each of these integral surfaces. This method enables the calculation of all noise sources referenced in the Lighthill formulation, including quadrupole noise that is generated due to turbulence-turbulence interaction during the mixing of the jet at the nozzle exit and dipole noise that is caused by unsteady fluctuations of the surface. The second method used is the impermeable FW-H formulation, which considers the surface of the flat plate as the FW-H surface and an acoustic source. This method only captures the noise contribution due to unsteady surface loading or dipole noise sources. By analyzing the noise prediction using both methods, we can gain insight into the significance of quadrupole and dipole noise sources.

Fig. 11 shows the SPL comparison for isolated and installed SMC000, SMC002, and SMC006 nozzles at Mach numbers of 0.4 and 0.7, using the permeable FW-H method. The noise spectrum is presented at three polar angles of 30°, 60°, and 90° for Strouhal numbers ranging from 0.03 to 2.0. The noise calculated using the permeable FW-H method exhibits good agreement with the experimental measurements for all nozzles at both Mach numbers, indicating that the LES solution, in conjunction with the FW-H surfaces, as shown in Fig. 5, accurately computes the noise.

The spectrum for the installed jet is accurately predicted for all nozzles at both Mach numbers and all observer angles. However, for the isolated jet simulations, a low-frequency discrepancy is observed at low Mach number (i.e. Mach = 0.4) as can be seen in Figs. 11a, 11c and 11e. The low frequency discrepancy can be associated with the fact that they are associated with the large scale eddies developing in the downstream location and have larger-time scales, requiring the numerical simulation to be run for longer time-periods. For the current case, the simulations are run for 2000 flow time-units (TUs). Hence the low-frequency discrepancy can be improved by simulating the flow for longer flow TUs. Nonetheless, these result highlights that the mesh generated near the nozzle exit, along with additional refinement at the lip line and conical refinement until $15D_j$ in the downstream region, accurately resolves the eddy structures responsible for the noise at all frequencies of interest.

In addition, the spectral characteristics of the isolated and installed jet configurations are compared in Fig. 11. It is observed that the jet installation noise exhibits a distinctive feature of spectral amplification at low Strouhal numbers. This amplification is more significant at a polar angle of 90° compared to 30°. For example, at Mach = 0.4, the spectral amplification at a polar angle of 90° is observed to be 12-14 dB, while at a polar angle of 30°, the amplification is only 3-5 dB. This observation provides important insights into the characteristics of jet-installation noise, which shows that jet-installation noise is more dominant at 90° polar angle in comparison with 30°, in line with the existing results (Brown and Wernet, 2014; Jawahar et al., n.d.). The noise amplification shows that the unsteady loading and the edge-scattering phenomenon is dominating factor at 90° polar angle, which according to (Lyu and Dowling, n.d.), is mentioned as being caused dominant dipole source. The above results also suggest that the LES grid and the placement of the permeable FW-H surface were sufficient to capture the underlying physics of jet installation.

To investigate the dominance of the dipole source, the installed jet noise is predicted using the impermeable FW-H method, whereby the pressure fluctuations on the flat plate are considered as the acoustic source. The comparison of the permeable and impermeable FW-H method is shown for SMC000 at Mach = 0.4 and 0.7 in Fig. 12. The results indicate that the prediction using the impermeable FW-H method is dependent on the polar angle, Mach number, and Strouhal number range of the noise computation. For example, at Mach = 0.4, the noise spectrum is accurately predicted over the entire Strouhal number for 60° and 90°, while only the low-Strouhal number amplification is accurately predicted with discrepancies up to 5 to 7dB observed at the high-Strouhal number for the 30° polar angle. The same pattern is observed at Mach 0.7, with only the noise prediction at 60° and 90° being accurately predicted, while the entire frequency range for 30° is under-predicted. This observation is also noted for the SMC002 and SMC006 nozzles. This signifies an interplay between the dominance of quadrupole and dipole noise, which depends on the Mach number and observer angle. For the installed jet

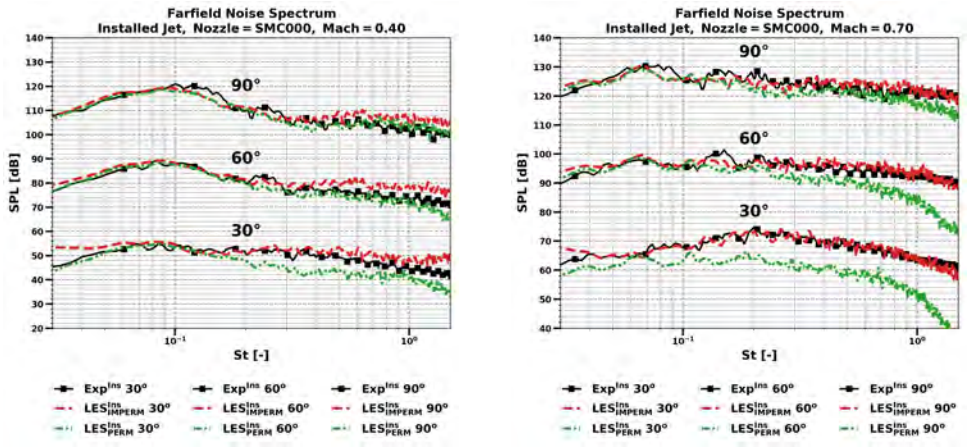

(a) Mach = 0.4 (b) Mach = 0.7

Figure 12 Comparison of noise predictions for the installed SMC000 nozzle at Mach numbers 0.4 and 0.7 using the permeable and impermeable FW-H methods.

noise, the noise due to dipole surface loading is dominant at higher polar angles, regardless of the Mach number, while the noise due to the quadrupole source is dominant at low polar angles, such as 30°, as the deviation between the measurement and the prediction increases as the Mach number increases. This is further analysed by comparing the polar plot of the noise predicted using both formulations of the FW-H with the experimental measurement, which is given in Figs. 14b, 14d and 14f. The results show that the permeable FW-H formulation has been able to accurately predict the noise for all nozzles and Mach number, while a slight discrepancy was observed in low polar angles. Furthermore, the results also show that impermeable FW-H formulation has also only been able to capture noise for polar angles greater than 60°, signifying that contribution due to dipole source is mostly contributing to the total noise at a higher polar angle while the influence of quadrupole source being dominant at low polar angles.

Figs. 14a, 14c and 14e shows the polar plot of the OASPL for round and chevron nozzles for the isolated jet. The OASPL plots for all nozzles show good agreement with the experimental measurements across all polar angles. The noise directivity predicted by the simulation follows the same trend as the experimental data, with highly directive noise observed in the downstream direction of the jet. This observation aligns with previous studies (Bridges and Brown, n.d.; Lawrence et al., 2011; L., 2017) that have attributed the downstream directivity of jet noise to the convective effect of the flow, with peak noise observed at a polar angle of 30°. However, minor differences in the magnitude of OASPL for the SMC000 nozzle at Mach 0.4 and for the SMC002 nozzle at Mach 0.7 are observed, which may be attributed to a slight overestimation at low strouhal number for the SMC000 nozzle and slight underestimation of high strouhal number for the SMC002 nozzle.

The results presented in Fig. 11 also demonstrate the effectiveness of the chevron nozzle in modifying the noise signature of the jet in comparison to the round nozzle. For the installed jet, a noticeable reduction in spectral levels is observed for SMC006 at 90° observer angle, where the low Strouhal number amplification at Mach 0.4 is reduced to 8dB, compared to 10dB for the round nozzle. On the other hand, SMC002 shows higher noise levels. These observations suggest that the chevron nozzle modifies the far-field noise radiation pattern of the jet. The peak amplitude of the noise spectrum remains relatively unaffected by the nozzle type, with the peak at Mach=0.4 occurring at a Strouhal number of 0.1 to 0.12 and the peak at Mach 0.7 occurring at 0.08 Strouhal number. These findings highlight the potential of the chevron nozzle to alter the character of the noise spectrum. However, further research is necessary to investigate the influence of the chevron geometric parameters on the noise of the installed jet.

To investigate the impact of chevrons on the generated noise in isolated and installed setups, the OASPL calculated for the chevron nozzles is subtracted from the OASPL of the round nozzle for observer angles ranging from 30 to 120 degrees and Mach numbers ranging from 0.3 to 0.9. The comparison is shown in Fig. 13, which shows that the SMC002 chevron nozzle produces more noise than the round jet for both setups. The increase in noise is influenced by both the acoustic Mach number and observer angle. For instance, for installed setup, a higher noise level is observed at a 30° polar angle for low Mach numbers, such as 2.5 dB at Mach=0.4, which shifts towards a 120° polar angle at higher Mach numbers, such as 3.5 dB at Mach=0.9. As such, the overall acoustic disadvantages range between 0.5 dB to 3.5 dB for the entire range of Mach numbers and observer angles. A similar trend is observed for SMC002 in an isolated setup with a maximum difference in the noise level of 2dB with the round jet.

Furthermore, Fig. 13d also shows the difference of OASPL by SMC006 chevron with a round nozzle. The findings demonstrate that the SMC006 chevron nozzle decreases noise, but the noise reduction is highly dependent on the Mach number. For instance, the SMC006 nozzle installed configuration reduces noise compared to the round nozzle for all observer angles at Mach numbers up to 0.7. However, for Mach numbers of 0.8 and 0.9, the acoustic benefit reduces at

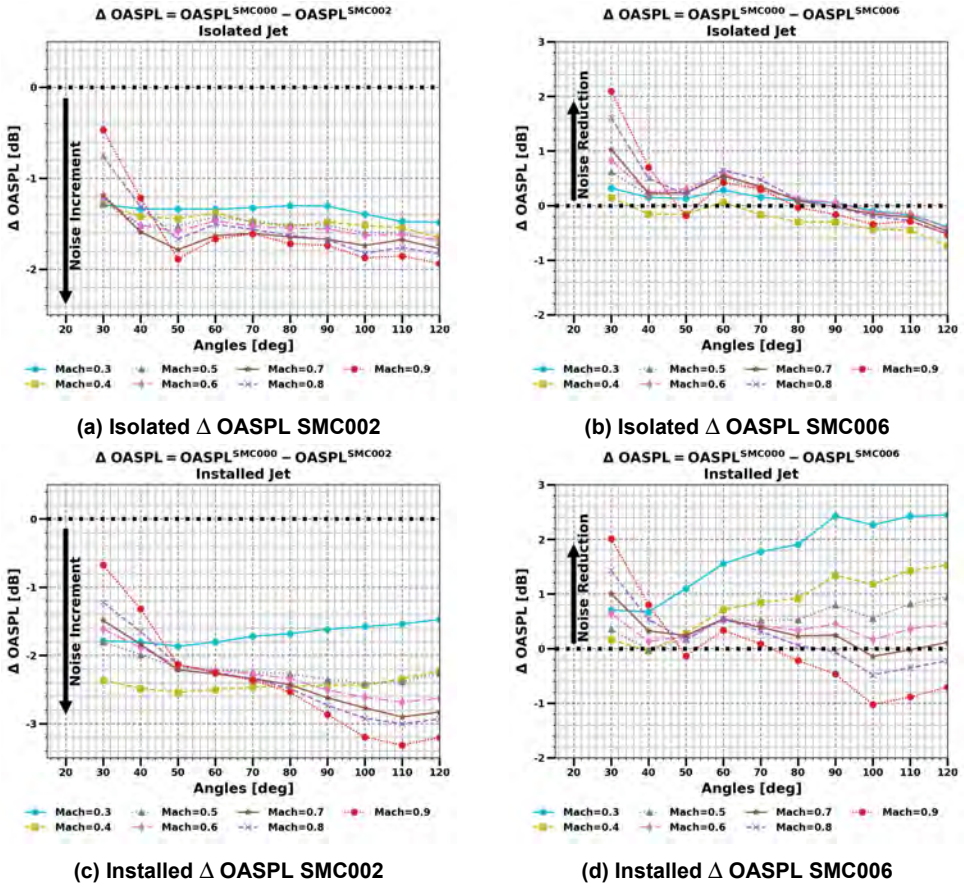

(a) Isolated Δ OASPL SMC002 **(b) Isolated Δ OASPL SMC006**

(c) Installed Δ OASPL SMC002 **(d) Installed Δ OASPL SMC006**

Figure 13 Comparison of OASPL for SMC002 and SMC006 chevron nozzles with SMC000 at various Mach numbers and polar angles in isolated and installed configuration

observer angles above 90°, and an increase in noise of 1.2 dB is observed. This is in contrast with the noise spectrum for SMC006 in an isolated configuration, whereby it is observed that acoustic benefits were limited to observer angles less than 90° for all Mach numbers. This signifies that the acoustic benefits of SMC006 are not only observed in isolated setup but increase when a plate is installed underneath it, as the noise can be reduced for the entire observer angle. However, noise increment for SMC006 is more in the installed setup (i.e., 1.2dB) in comparison with the isolated setup, where it is a maximum of 0.5 dB. This further highlights that it is important to incorporate a well-defined objective function regarding the polar angle in the noise reduction methodology.

The study also involves calculating the aerodynamic performance of the SMC000, SMC002, and SMC006 to analyze how the addition of chevrons impacts the generated thrust. The thrust is calculated using Eq. (3) where subscript e represents the value obtained at the nozzle exit and a represents the atmospheric value.

$$T = \rho_e U_e^2 A_e + (P_e - P_a) A_e \tag{3}$$

The thrust calculation requires the effective exit area A_e, which is straightforward for the round nozzle, however, the thrust calculation for the chevron nozzle is problematic due to the difficulty in characterising the effective thrust area. A surrogate area measurement was utilised in Yang et al. (n.d.) to establish an effective nozzle diameter by measuring the mass flow. Thus, in the current study, the thrust value is measured directly on a cross-flow slice downstream of the nozzle exit at an axial distance of $x = 0.1D_j$. The thrust is only calculated for Mach = 0.5. Table 2 shows the calculation of the thrust and shows that SMC002 results in increased thrust, in comparison with SMC000 and SMC006. The increased thrust by SMC002 is owed to the 5degree penetration angle by the chevron, resulting in increased area and corresponding mass flow rate. Hence while SMC002 results in increased thrust, it also results in the increase noise in isolated and installed configuration.

Overall, the LES CABARET solver has been able to predict the noise generated by the installed round and chevron jets for Mach numbers ranging from 0.3 to 0.9 with considerable accuracy, particularly for the 90° polar angle. Additionally, the advantage of employing a chevron in reducing jet installation noise is dependent not only on the type of chevron (i.e. the number of chevrons, penetration length, and penetration angle) but also on the jet flow conditions.

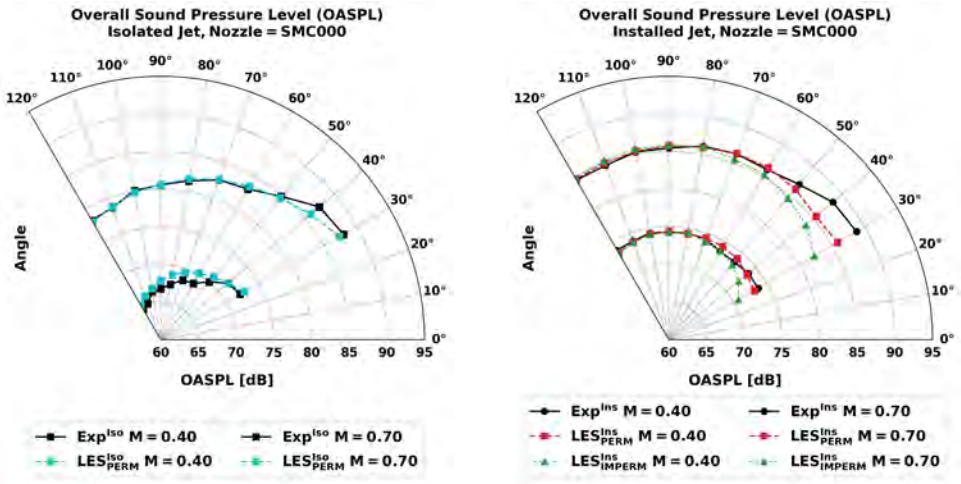

(a) Isolated SMC000

(b) Installed SMC000

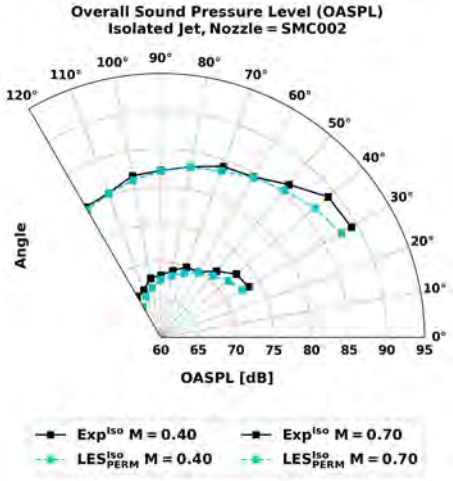

(c) Isolated SMC002

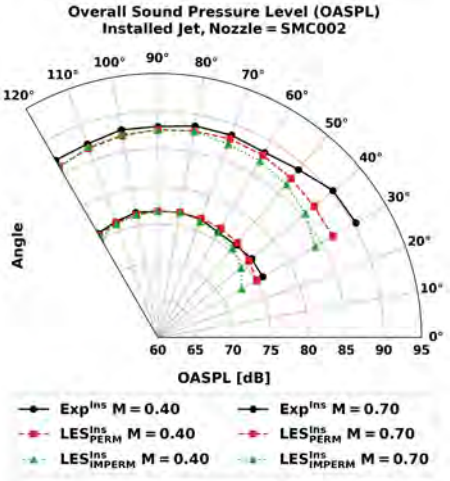

(d) Installed SMC002

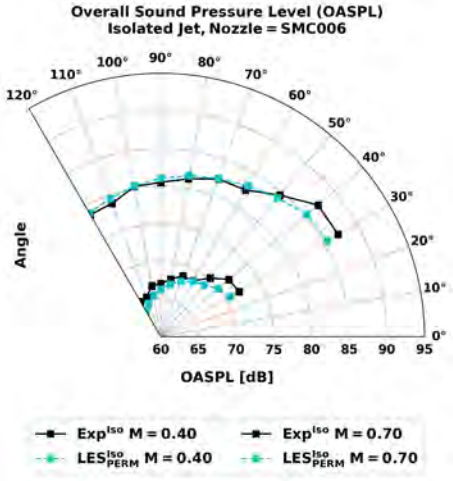

(e) Isolated SMC006

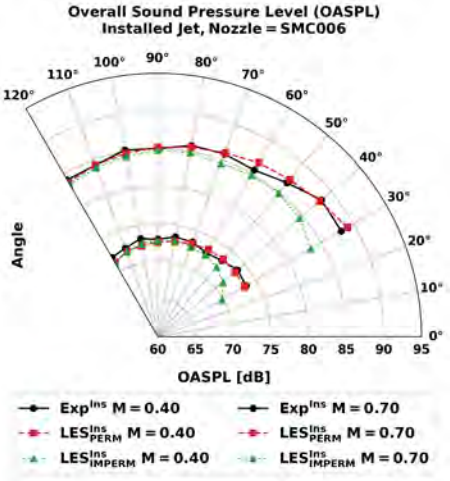

(f) Installed SMC006

Figure 14 Comparison of experimental and predicted noise for SMC000, SMC002, and SMC006 nozzles at Mach 0.4 and 0.7 in isolated and installed jet conditions using permeable and impermeable FW-H method

2.3 Velocity scaling

The acoustic power scaling of the installed configurations is based on scaling the OASPL plots with the jet nozzle exit velocity to further analyze the effect of the chevron nozzle on the jet installation noise. For all the tested cases, the effect of inlet angle $\theta = 90^\circ$ is presented in Fig. 15a, to neglect the refraction effects and directly compare with the Lighthill theory

Table 2 Calculation of thrust and mass flow rate and exit area for SMC000, SM002 and SMC006

Nozzle	Thrust(N)	Mass flow rate (kg/s)	A_e(mm^2)
SMC000	8.29	0.053	274.39
SMC002	9.16	0.062	337.37
SMC006	7.34	0.051	331.83

(Lighthill, 1952, 1954). According to the latter, the far-field acoustic power of jet noise is proportional to the eighth power of the jet velocity at the nozzle exit, U_j^8, for cold jets at $\theta = 90°$. Fig. 15 compares the velocity scaling of the isolated jet from the present study with that of NASA (Brown, 2013), and (Kamliya Jawahar et al., 2023). The results demonstrate excellent agreement with the theory, indicating that the jet noise from the present study scales with $U_j^{7.9}$ at $\theta = 90°$. This result is in-line with previous experimental studies (Brown, 2013; Rego et al., 2021; Brown and Bridges, 2006; Khavaran and Bridges, 2009; Bailly et al., 2016) for the isolated jets.

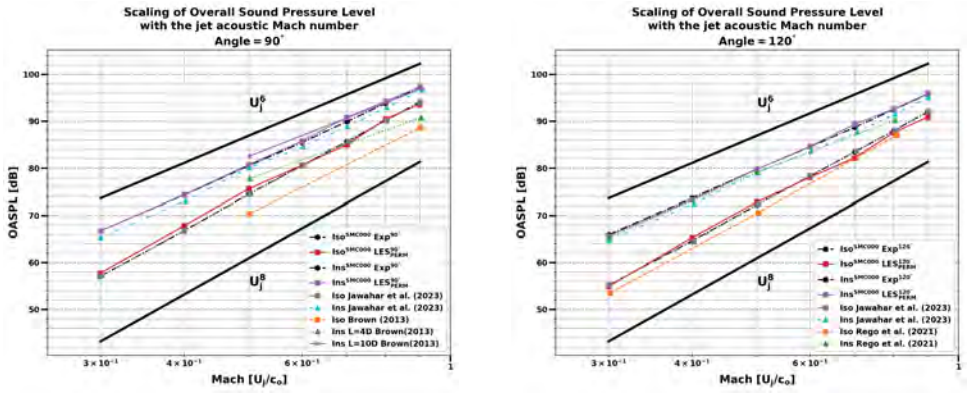

(a) $\theta = 90°$ **(b)** $\theta = 120°$

Figure 15 Comparison of the scaling of Overall Sound Pressure Level with the jet acoustic Mach number for SMC000 isolated and installed jet configurations at two different angles. (a) Results at $\theta = 90°$ are compared with previous studies by (Brown, 2013) and (Kamliya Jawahar et al., 2023), while (b) results at $\theta = 120°$ are compared with the study by (Rego et al., 2021) and (Kamliya Jawahar et al., 2023).

In Figs. 15a and 15b, the velocity scaling plot for both the current LES and experimental results of the installed jet for the baseline configuration displays a dipole-like scaling of U_j^6, which is predicted for the case of high fluid loading on the surface (Curle, 1955). Previous experimental studies, such as (Brown, 2013) and (Kamliya Jawahar et al., 2023) using a long flat-plate to study the jet installation effects, have also found similar scaling laws between U_j^5 and U_j^6. (Brown, 2013) and (Lawrence, 2014) conducted experiments demonstrating a velocity scaling close to U_j^5 for short surfaces and U_j^6 for longer surfaces. (Lawrence, 2014) documented a transition region from U_j^5 to U_j^6 when the surface extends downstream. In Fig. 15b, the results for the installed and isolated cases at upstream angle $\theta = 120°$ from the present study are compared with $\theta = 140°$ from experiments conducted by (Rego et al., 2021), who demonstrated a scaling close to U_j^6 for the installed jet. The present study validates this observation, as the installed configuration at $\theta = 120°$ also displays a U_j^6 velocity scaling, which is in agreement with the study conducted by (Rego et al., 2021) for upstream angles (see Fig. 15b).

Fig. 16 presents the velocity exponents n of the OASPL scaling with the jet velocity for different inlet angles. It is observed that Lighthill's power law is no longer a good predictor of acoustic power at inlet angles close to the jet axis in the flow direction, even for isolated jets, due to the mean flow propagation effects. For isolated jets at inlet angles towards the jet axis, the velocity exponent n increases to U_j^9, as reported in previous studies (Bailly et al., 2016; Brown and Bridges, 2006; Khavaran and Bridges, 2009). At higher inlet angles, the increase in energy of jet noise is attributed to Lighthill's convective amplification, which efficiently propagates noise in a spreading jet flow at low frequencies that correspond to the peak jet noise (Goldstein et al., 2012). The acoustic power scaling for Chevron nozzles in installed configurations is analyzed, and it is found that at upstream angle $\theta = 120°$, the scaling exponent increases from $U_j^{6.2}$ to $U_j^{6.8}$ for Chevron nozzles, while at $\theta = 90°$, the scaling exponent increases from $U_j^{6.4}$ to U_j^7. However, at the downstream location of $\theta = 30°$, the Chevron nozzles show a slightly lower exponent of $U_j^{8.2}$ compared to the round jet with an exponent of $U_j^{8.6}$. In the isolated configuration, the chevrons do not exhibit a significant difference in the velocity exponent compared to the round nozzle. Nevertheless, at the downstream angle of $\theta = 30°$, the chevron shows a lower velocity exponent of $U_j^{8.7}$ compared to a round jet of $U_j^{9.1}$. Overall, the above results clearly show that the application of chevron nozzles reduces the effect of jet installation effect which could be owed to the modification of the near field hydrodynamic field.

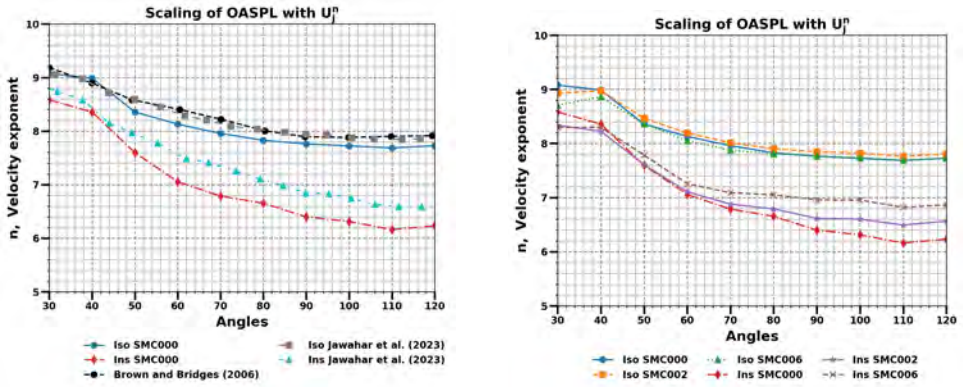

(a) (b)

Figure 16 Comparison of the velocity exponent for various inlet angles across all tested configurations, in comparison with the isolated configuration of (Brown and Bridges, 2006) and isolated and installed configuration from (Kamliya Jawahar et al., 2023).

3 CONCLUSION

A computational investigation employing Large Eddy Simulation (LES) was undertaken to model jet mixing and installation noise of round (SMC000) and chevron nozzles (SMC002 and SMC006) at acoustic Mach numbers varying from 0.3 to 0.9. The LES computations employed the high-resolution CABARET method accelerated with Graphics Processing Units. The numerical simulations were based on experiments performed at the University of Bristol, featuring a simplified installed jet configuration with a plate beneath the jet with $H/D_j = 2$ and $L/D_j = 6.5$. The far-field noise was computed from the LES solver in conjunction with the Ffowcs Williams and Hawking (FW-H) method. Two formulations of the FW-H method were employed to model the jet installation noise: the permeable FW-H and impermeable FW-H methods. The goal of the investigation was to analyse the effect of quadrupole and dipole noise for round and chevron nozzles and the interplay of these sources depending on the Mach number and observer angle. The predicted far-field noise spectra were compared to experimental measurements for all nozzle types at two Mach numbers and three polar angles (30°, 60°, and 90°), exhibiting good agreement. The Band Limited (BL) Overall Sound Pressure Level (SPL) were also computed to show that the LES-FWH solution was within 1-2dB of the experimental measurement. The results indicate that SMC006 results in reduced noise compared to SMC000, while SMC002 leads to increased noise. It is also shown that the noise reduction advantage of SMC006 decreases with increasing Mach number. For the installed jet noise calculations, it was shown that the permeable FW-H method accurately captures the jet installation noise for the entire frequency range for all chevrons and polar angles. In comparison with this, the impermeable FW-H method, which only comprised contributions due to the dipole source, can only more-or-less capture jet-installation noise at 60° and 90° polar angles. This confirms that at higher polar angles, the dipole source is the most dominant mechanism of jet noise, while at shallow polar angles, the contribution from the quadrupole source is more pronounced and increases with the Mach number. The effects of chevron nozzles on jet installation noise were analyzed by scaling the acoustic power with the jet velocity at the nozzle exit. At upstream angle $\theta = 120°$, chevron nozzles had a higher scaling exponent than round nozzles, while at $\theta = 90°$, the scaling exponent also increased. However, at the downstream location of $\theta = 30°$, chevron nozzles showed a slightly lower exponent. In isolated configurations, chevrons did not exhibit a significant difference in the velocity exponent compared to round nozzles. Overall, chevron nozzles, especially SMC006, reduce the effect of jet installation noise by changing the noise character to a more like the quadrupole source of isolated jet noise. This is attributed to the change which the chevron-induced mixing produces for the linear hydrodynamic field of the jet flow.

References

Abid, H. A., Markesteijn, A. P. and Karabasov, S. A. (2021), *Trailing Edge Noise Modelling of Flow over NACA Airfoils Informed by LES*, American Institute of Aeronautics and Astronautics.
URL: *https://arc.aiaa.org/doi/abs/10.2514/6.2021-2233*

Abid, H. A., Stalnov, O. and Karabasov, S. A. (2021), *Comparative Analysis of Low Order Wall Pressure Spectrum Models for Trailing Edge Noise Based in Amiet Theory*, American Institute of Aeronautics and Astronautics.
URL: *https://arc.aiaa.org/doi/abs/10.2514/6.2021-2231*

Bailly, C., Bogey, C. and Castelain, T. (2016), 'Subsonic and supersonic jet mixing noise—in measurement', *Simulation and control of subsonic and supersonic jet noise. von Karman Institute for Fluid Dynamics* .

Bridges, J. and Brown, C. (n.d.), *Parametric Testing of Chevrons on Single Flow Hot Jets*.
URL: *https://arc.aiaa.org/doi/abs/10.2514/6.2004-2824*

Brown, C. A. (2013), 'Jet-surface interaction test: Far-field noise results', *Journal of Engineering for Gas Turbines and Power* **135**(7), 071201.

Brown, C. A. and Wernet, M. P. (2014), 'Jet-surface interaction test: Flow measurement results', *20th AIAA/CEAS Aeroacoustics Conference* .

Brown, C. and Bridges, J. (2006), 'Small hot jet acoustic rig validation'.
URL: *http://www.sti.nasa.gov*

Chintagunta, A., Naghibi, S. and Karabasov, S. (2018), 'Flux-corrected dispersion-improved cabaret schemes for linear and nonlinear wave propagation problems', *Computers and Fluids* **169**, 111–128. Recent progress in nonlinear numerical methods for time-dependent flow and transport problems.

Curle, N. (1955), 'The influence of solid boundaries upon aerodynamic sound', *Proceedings of the Royal Society of London. Series A. Mathematical and Physical Sciences* **231**(1187), 505–514.

Faranosov, G. A., Goloviznin, V. M., Karabasov, S. A., Kondakov, V. G., Kopiev, V. F. and Zaitsev, M. A. (2013), 'Cabaret method on unstructured hexahedral grids for jet noise computation', *Computers and Fluids* **88**, 165–179.
URL: *https://www.sciencedirect.com/science/article/pii/S0045793013003289*

Goldstein, M., Sescu, A. and Afsar, M. (2012), 'Effect of non-parallel mean flow on the green's function for predicting the low-frequency sound from turbulent air jets', *Journal of fluid mechanics* **695**, 199–234.

Head R., F. M. (n.d.), *Jet/surface interaction noise - Analysis of farfield low frequency augmentations of jet noise due to the presence of a solid shield*.
URL: *https://arc.aiaa.org/doi/abs/10.2514/6.1976-502*

Hoheisel, H. and Frhr. von Geyr, H. (2012), 'The influence of engine thrust behaviour on the aerodynamics of engine airframe integration', *CEAS Aeronaut J* **3**(1-4), 79–92.

Jawahar, H. K., Markesteijn, A. P., Karabasov, S. A. and Azarpeyvand, M. (n.d.), *Effects of Chevrons on Jet-installation Noise*.
URL: *https://arc.aiaa.org/doi/abs/10.2514/6.2021-2184*

Jordan, P., Jaunet, V., Towne, A., Cavalieri, A. V. G., Colonius, T., Schmidt, O. and Agarwal, A. (2018), 'Jet–flap interaction tones', *Journal of Fluid Mechanics* **853**, 333–358.

Kamliya Jawahar, H. and Azarpeyvand, M. (2021), Trailing-edge treatments for jet-installation noise reduction, *in* 'AIAA AVIATION 2021 FORUM', p. 2185.

Kamliya Jawahar, H. and Azarpeyvand, M. (2022), On investigating the hydrodynamic field for jets with and without installation effects, *in* 'AIAA AVIATION 2022 FORUM'.

Kamliya Jawahar, H., Baskaran, K. and Azarpeyvand, M. (2021), Unsteady characteristics of mode oscillation for\screeching jets, *in* 'AIAA AVIATION 2021 FORUM', p. 2279.

Kamliya Jawahar, H., Karabasov, S. A. and Azarpeyvand, M. (2023), 'Jet installation noise reduction using porous treatments', *Journal of Sound and Vibration* **545**, 117406.
URL: *https://www.sciencedirect.com/science/article/pii/S0022460X22005892*

Kamliya Jawahar, H., Meloni, S., Camussi, R. and Azarpeyvand, M. (2021), Experimental investigation on the jet noise sources for chevron nozzles in under-expanded condition, *in* 'AIAA AVIATION 2021 FORUM', p. 2181.

Karabasov, S. and Goloviznin, V. (2009), 'Compact accurately boundary-adjusting high-resolution technique for fluid dynamics', *Journal of Computational Physics* **228**, 7426–7451.

Khavaran, A. and Bridges, J. (2009), Shjar jet noise data and power spectral laws, Technical report, NASA TM-2009-215608.

L., B. (2017), 'Experimental investigation of the far-field noise due to jet-surface interaction combined with a chevron nozzle', *Appl. Acoust.* **127**, 240.

Lawrence, J. (2014), Aeroacoustic interactions of installed subsonic round jets, *in* 'University of Southampton', p. 275.

Lawrence, J., Azarpeyvand, M. and Self, R. (2011), *Interaction between a Flat Plate and a Circular Subsonic Jet*.
URL: *https://arc.aiaa.org/doi/abs/10.2514/6.2011-2745*

Lighthill, M. J. (1952), 'On sound generated aerodynamically i. general theory', *Proceedings of the Royal Society of London. Series A. Mathematical and Physical Sciences* **211**(1107), 564–587.

Lighthill, M. J. (1954), 'On sound generated aerodynamically ii. turbulence as a source of sound', *Proceedings of the Royal Society of London. Series A. Mathematical and Physical Sciences* **222**(1148), 1–32.

Lyu, B. and Dowling, A. (n.d.), *Noise Prediction for Installed Jet*.
URL: *https://arc.aiaa.org/doi/abs/10.2514/6.2016-2986*

Markesteijn, A. P., Gryazev, V., Karabasov, S. A., Ayupov, R. S., Benderskiy, L. A. and Lyubimov, D. A. (2020), 'Flow and noise predictions of coaxial jets', *AIAA Journal* **58**(12), 5280–5293.

Markesteijn, A. P. and Karabasov, S. A. (2018), 'Cabaret solutions on graphics processing units for nasa jets: Grid sensitivity and unsteady inflow condition effect', *Comptes Rendus Mécanique* **346**(10), 948–963. Jet noise modelling and control / Modélisation et contrôle du bruit de jet.
URL: *https://www.sciencedirect.com/science/article/pii/S1631072118301505*

Markesteijn, A. P. and Karabasov, S. A. (2019), 'Simulations of co-axial jet flows on graphics processing units: the flow and noise analysis', *Philosophical Transactions of the Royal Society A: Mathematical, Physical and Engineering Sciences* **377**(2159), 20190083.
URL: *https://royalsocietypublishing.org/doi/abs/10.1098/rsta.2019.0083*

Mead, C. and Strange, P. (1998), 'Under-wing installation effects on jet noise at sideline', *4th AIAA/CEAS Aeroacoustics Conference* .
URL: *https://arc.aiaa.org/doi/abs/10.2514/6.1998-2207*

Mukha, T., Rezaeiravesh, S. and Liefvendahl, M. (2019), 'A library for wall-modelled large-eddy simulation based on OpenFOAM technology', *Computer Physics Communications* **239**, 204–224.

Park, I. G. (2015), 'Wall-modeled large-eddy simulation of a separated flow over the NASA wall-mounted hump', *Annual Research Briefs (Center for Turbulence Research)* (2006), 145–160.

Rego, L., Ragni, D., Avallone, F., Casalino, D., Zamponi, R. and Schram, C. (2021), 'Jet-installation noise reduction with flow-permeable materials', *Journal of Sound and Vibration* **498**, 115959.

Semiletov, V. A. and Karabasov, S. A. (2018), 'A volume integral implementation of the goldstein generalised acoustic analogy for unsteady flow simulations', *Journal of Fluid Mechanics* **853**, 461–487.

Semiletov, V. and Karabasov, S. (2013), 'Cabaret scheme with conservation-flux asynchronous time-stepping for nonlinear aeroacoustics problems', *Journal of Computational Physics* **253**, 157–165.

Semiletov, V. and Karabasov, S. (2014), 'Cabaret scheme for computational aero acoustics: Extension to asynchronous time stepping and 3d flow modelling', *International Journal of Aeroacoustics* **13**(3-4), 321–336.
URL: *https://doi.org/10.1260/1475-472X.13.3-4.321*

Shearin, J. G. (1983), 'Investigation of jet-intallation noise sources under static conditions', *Technical Report 2181, NASA Technical paper.* .

Tucker, P. G. and Karabasov, S. A. (2009), 'Unstructured grid solution of the eikonal equation for acoustics', *International Journal of Aeroacoustics* **8**(6), 535–553.
URL: *https://doi.org/10.1260/147547209789141498*

Way, D. and Turner, B. (1980), 'Model tests demonstrating under-wing installation effects on engine exhaust noise', *6th Aeroacoustics Conference* .

Yang, G., Allen, C. B., Markesteijn, A. P., Abid, H. A., Karabasov, S. A. and Toropov, V. V. (n.d.), *Surrogate Model-Based Acoustic Optimisation of Jet Nozzle Exit Geometry*.
URL: *https://arc.aiaa.org/doi/abs/10.2514/6.2022-0683*